

Numerical Investigations of Hydrodynamic Performance of a NACA0012 Hydrofoil in Water-Air-Bubble Mixed Flows

Kangjian He¹, Cong Ye^{1,2}, Decheng Wan^{1}*

¹ Computational Marine Hydrodynamics Lab (CMHL), School of Naval Architecture, Ocean and Civil Engineering, Shanghai Jiao Tong University, Shanghai, China

² China Ship Scientific Research Center, Shanghai, China

*Corresponding author

ABSTRACT

Water-air-bubble mixed flow is a complex multiphase flow generated by the intense interaction between marine structures and surrounding fluids. It involves remarkable and complicated influence on the hydrodynamic performance of marine structures. This paper studied the influence of uniformly mixed water-air-bubble incoming flow on hydrodynamic performance of a two-dimensional NACA0012 hydrofoil by using the Computational Fluid Dynamics (CFD) method. Two-fluid method (TFM) is adopted to solve the mixed water-air-bubble multiphase flow field with the open-source CFD toolkit OpenFOAM. Validation of the numerical model is conducted in two aspects. On the one hand, numerical results with single-phase incoming water flow are compared with experimental and numerical results in literatures. On the other hand, mesh convergence test is conducted to further verify the convergence and robustness of this model. On the basis, the influence of water-air-bubble flow for the condition of 10% air volume fraction on velocity and pressure fields around the hydrofoil is presented. Coefficients of lift and drag of the hydrofoil are discussed comparing with single-phase water flow condition. This research can provide a valuable reference for studying the complex interaction between multiphase water-air-bubble mixed flow and marine structures.

KEY WORDS: Water-air-bubble mixed flow; two-fluid method; hydrofoil; hydrodynamic performance.

INTRODUCTION

Water-air-bubble mixed flow is a complicate multiphase flow and usually generated by the intense interactions between navigating ships and free surface flow. Water-air-bubble mixed flow usually involves lots of bubbles with multiple sizes and little-scale interface. Lots of bubbles in the water-air-bubble mixed flow will sweep down along the ship and cluster near the propulsion system, which will affect the hydrodynamic performance of hull-propeller-rudder. The cavitation of propeller will generate cavitation bubbles and effects the hydrodynamic performance of the rudder. Otherwise, the submarine usually set holes at the stern to release flue gas. The flue gas released from holes will generate water-air-bubble mixed flow, which changes the back flow

field and affects the hydrodynamic performance of rudder and propeller. The effect on the hydrodynamic performance of marine structures, such as propeller performance and ship maneuverability, is complicated and unclear. It is significant to adopt multiphase method to study complicated water-air-bubble mixed flow and analyze the effect.

Numerical simulation has been widely adopted to model the multiphase flow. There are three main multiphase method: interface capture method, Euler-Lagrange method, and Euler-Euler method. Interface capture method such as Volume of Fluid (VOF) method (Hirt and Nichols, 1981) and Level-Set method (Carrica et al., 2007) is the most commonly used method in naval architecture and ocean engineering, which involves large-scale water-air interface (Zhang et al., 2020). However, this method usually requires finer mesh resolution relative to the scale of water-air interface to accurately capture the physical process (Wardle and Weller, 2013). Euler-Lagrange method (Ma et al., 2015) uses spherical Lagrange particles to model micro bubbles and solves the liquid phase based on Euler method. Euler-Lagrange method provides a relatively precise method to model multiphase flow and can capture the detail motion of bubbles (Zhang et al., 2020). However, this method will require high computational cost with the increasing number of Lagrange particles. Euler-Euler method, or two-fluid method (TFM) treats the dispersed phase as continuous and solve the dispersed phase with Navier-Stokes equations. TFM is adaptive to be used to model high air volume fraction multiphase flow due to relatively low computational cost. TFM has been broadly validated and applied in the simulation of bubble columns (Adam Mühlbauer, et al., 2019), bubble flow around the ship (Li et al., 2019; Ma et al., 2011), and other complex two-phase flows. Water-air-bubble mixed flow usually involves numerous micro bubbles and micro-scale water-air interface. It is difficult to be modeled with interface capture method and Euler-Lagrange method. Therefore, TFM is adopted to model the water-air-bubble mixed flow in this paper.

This paper is organized as follows: The numerical computational method and calculation settings are introduced first. Then, the validation and verification are conducted to show the correctness of the computational method. Finally, the influence of uniformly mixed water-air-bubble incoming flow on hydrodynamic performance is discussed and conclusions are summarized.

NUMERICAL APPROACH

Computational Method

TFM is adopted to solve the mixed water-air-bubble multiphase flow field. TFM is based on a Eulerian-Eulerian two-fluid solution framework. The liquid phase is treated as the continuum phase while the gas phase is considered as the dispersed phase. Mass and momentum conservation equations are solved for each phase. The heat transfer between two phase is not considered and two phases are incompressible and immiscible in this paper.

The governing equations are mass and momentum conservation equations and written as:

$$\frac{\partial \alpha_i}{\partial t} + \nabla \cdot (\alpha_i \mathbf{u}_i) = 0 \quad (1)$$

$$\frac{\partial \alpha_i \mathbf{u}_i}{\partial t} + \nabla \cdot (\alpha_i \mathbf{u}_i \mathbf{u}_i) + \nabla \cdot (\alpha_i \mathbf{R}_i^{eff}) = -\frac{\alpha_i}{\rho_i} \nabla p + \alpha_i \mathbf{g} + \frac{\sum \mathbf{F}_i}{\rho_i} \quad (2)$$

where the subscript i denotes different phases, in which $i=l$ and g represent the water phase and air phase, respective, α is the volume fraction, \mathbf{u} is the velocity, p is the pressure, \mathbf{g} is the gravity acceleration, and ρ is the density. \mathbf{R}^{eff} represents the effective Reynolds stress tensor and is calculated as:

$$\mathbf{R}_i^{eff} = -(\nu_i + \nu_i') \left[\nabla \mathbf{u}_i + (\nabla \mathbf{u}_i)^t - \frac{3}{2} \mathbf{I} \nabla \cdot \mathbf{u}_i \right] + \frac{3}{2} \mathbf{I} k_i \quad (3)$$

where ν represents the kinematic viscosity. The eddy-viscosity model is used in this paper and ν_i' denotes the turbulent kinematic viscosity.

\mathbf{I} represents the unit tensor and k is the turbulent kinematic energy.

$\sum \mathbf{F}$ represents interfacial forces to consider the interfacial momentum transfer between two phases. It includes the drag force \mathbf{F}_d , lift force \mathbf{F}_l , virtual mass force \mathbf{F}_{vm} , turbulent dispersion force \mathbf{F}_{td} , and wall lubrication force \mathbf{F}_{wl} . In this paper, we just consider the drag force and virtual force here.

The drag force \mathbf{F}_d is generated due to the relative motion between two phases. This force will be acted on the bubble when the bubble moves in the water. The drag force \mathbf{F}_d is calculated as:

$$\mathbf{F}_d = -\frac{3}{4} \alpha_g C_d \frac{\rho_l}{d_g} |\mathbf{u}_l - \mathbf{u}_g| (\mathbf{u}_g - \mathbf{u}_l) \quad (4)$$

where C_d is the coefficient of drag force and d_g is the diameter of bubbles. Many models have been proposed and validate by previous literatures (Adam Mühlbauer, et al., 2019). The drag force model proposed by (Schiller L. and Naumann A., 1935) is adopted in this paper, which the coefficient of drag force is calculated based on the bubble Reynolds number Re_d as follows:

$$C_D = \begin{cases} \frac{24}{Re_b} (1 + 0.15 Re_b^{0.687}), Re_b \leq 1000 \\ 0.44, Re_b > 1000 \end{cases} \quad (5)$$

where the bubble Reynolds number Re_d is defined according to the density, dynamic viscosity of liquid, bubble diameter, and relative velocity as:

$$Re_b = \frac{\rho_l |\mathbf{u}_l - \mathbf{u}_g| d_g}{\mu_l} \quad (6)$$

The virtual mass force is generated when the bubble accelerates in the water. The accelerated motion of bubble will cause the accelerating of surrounding fluid. The virtual mass force can be calculated as Eq.7 (Simcik et al., 2008; Zhang et al., 2006):

$$\mathbf{F}_{vm} = C_{vm} \alpha_g \rho_l \cdot \left(\frac{D\mathbf{u}_g}{Dt} - \frac{D\mathbf{u}_l}{Dt} \right) \quad (7)$$

where C_{vm} represents the coefficient of virtual mass force and the total derivate is defined as follows:

$$\frac{D}{Dt} = \frac{\partial}{\partial t} + \mathbf{u} \cdot \nabla \quad (8)$$

The constant coefficient model is always adopted in most related literatures and $C_{vm} = 0.5$ is confirmed for spherical bubbles in this paper.

The turbulence model is chosen as two-equation eddy-viscosity *SST k- ω* turbulence model based on the mixture phase using mixture properties. For more details about this turbulence model, please refer to Menter (1994).

TFM has been included in the incompressible multiphase solver *multiphaseEulerFoam* in the open-source CFD toolkit OpenFOAM v7. The solver *multiphaseEulerFoam* is adopted to solve the multiphase flow in this paper.

Geometric Model and Computational Domain

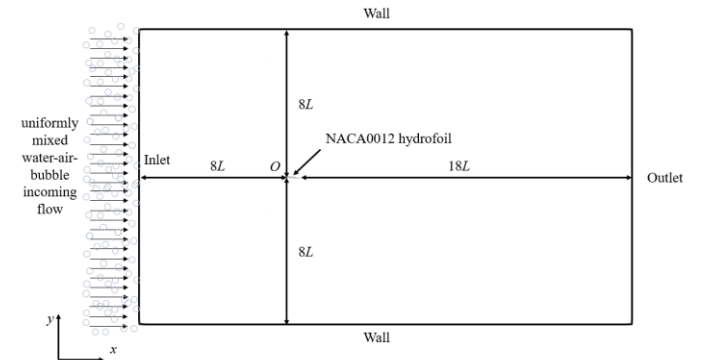


Fig.1 General layout of computational domain.

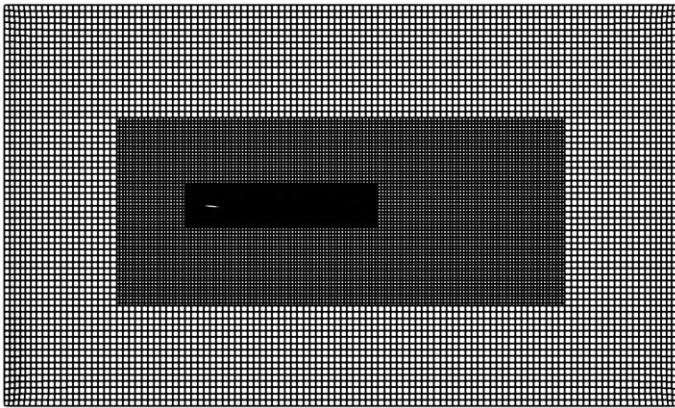
This paper takes a two-dimensional NACA0012 hydrofoil profile as the research object due to available convincing experimental (Ladson, 1988)

and numerical results (Shang and Horrillo, 2021) in single-phase incoming water coming flow condition.

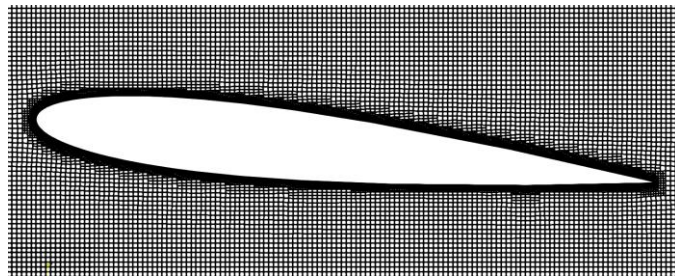
The general layout of computational domain is shown as Fig. 1 and the rectangular shape is used. The Cartesian coordinate $o-xy$ system is adopted and the origin is set at the head of the hydrofoil. The x and y axes are along the length and width directions of the computational domain, respectively. The length and width of the computational domain are set to be $27L$ and $16L$, respectively, where L is the chord length of the hydrofoil. The inlet boundary is located $8L$ upstream from the head of the hydrofoil. The outlet boundary is located $18L$ downstream from the trail of the hydrofoil. The side wall boundaries are located $8L$ from the hydrofoil. The distance can be considered as large enough to avoid the far field effect due to boundaries.

The mixed water-air-bubble incoming flow is generated at the inlet and propagates along x -positive direction. The mixed water-air-bubble incoming flow is assumed uniformly mixed at the inlet in this paper. To decrease the computational time, the mixed water-air-bubble flow is generated at the initial time $t=0s$ is at $x=-L$.

Mesh Distributions



(a) The overall meshes of computational domain



(b) Magnified view of partial meshes around the NACA0012 hydrofoil

Fig.2 Mesh distribution.

Unstructured mesh is adopted in this paper. The mesh is generated by the software Hexpress and then converted into the format that OpenFOAM can use. The overall mesh distribution is shown as Fig.2(a) and partial meshes around the NACA0012 hydrofoil is shown as Fig. 2(b). The prim mesh near the surface of the hydrofoil is used to better capture and analyze the flow field in the boundary layer. The first layer thickness of boundary layer is 0.00012 m and the stretching ratio is 1.2 . A finer mesh is used around the hydrofoil and wake zone to capture

detail flow characteristics. A relatively coarse mesh is used elsewhere to save the computational resources. The total number of meshes is $72\ 885$.

The timestep size is determined based on a prescribed Courant number (Co) value as follows:

$$Co = \frac{u\Delta t}{\Delta x} < 1 \quad (9)$$

where Δt is the timestep size, u is the normal velocity, and Δx is the distance between the cell centre and the centre of its neighbour cell.

Boundary Conditions

For the inlet boundary, the fixed value, $u_l = u_g = u_\infty$, is used for the velocity boundary condition. The fixed value boundary condition is applied for α_g and α_l . The *fixedFluxPressure* condition in OpenFOAM is used for the pressure condition. The turbulent kinetic energy k , turbulence specific dissipation rate ω and the turbulence viscosity ν_t is calculated as Eqs. 10~12:

$$k = \frac{3}{2}(I|u|)^2 \quad (10)$$

$$\omega = \frac{k^{0.5}}{C_\mu^{0.25}l} \quad (11)$$

$$\nu_t = \frac{a_1 k}{\max(a_1 \omega, SF_2)} \quad (12)$$

where I is the turbulence intensity, C_μ and a_1 are empirical constants in which $C_\mu = 0.09$ and $a_1 = 0.31$, and l is the turbulent reference length scale.

For the outlet boundary, the zero normal gradient condition is used for the velocity and volume fraction. The fixed value is used for the pressure boundary condition. The *inletOutlet* boundary condition is applied for α_g , α_l , k , and ω . The turbulence viscosity ν_t is calculated according to Eq. 12.

For the hydrofoil boundary, no-slip boundary condition is used for the velocity and the zero normal gradient condition is used for pressure, volume fraction and ω . For k and ν_t , the wall function method is applied for near wall region.

For the wall boundary, fixed value boundary condition, $u_l = u_g = u_\infty$, is used for the velocity. The zero normal gradient boundary condition is applied for the pressure, α_g , α_l , k , ν_t , and ω .

Calculation Conditions

The setting of calculation conditions about the velocity and angle of attack is based on the experiment of NACA0012 hydrofoil in single-phase incoming water flow condition. Parameters are summarized as Table.1

Table.1 Parameters of calculation conditions

Parameters	Unit	Value
Angle of attack of hydrofoil	degree	5.98
Chord length of hydrofoil L	m	1
Velocity of incoming flow u_∞	m/s	2.24
Kinematic viscosity of water ν_l	m ² /s	1.12×10^{-6}
Kinematic viscosity of air ν_l	m ² /s	1.46×10^{-5}

As the most important non-dimensional parameter, Reynolds number can be calculated as Eq. 13 and corresponding value is 200 000.

$$Re = \frac{u_\infty L}{\nu_l} \tag{13}$$

The bubble is assumed to be spherical and has constant diameter in this paper and $d = 0.5$ mm. The coalescence and break-up of bubbles are not considered in this paper. The volume fraction of air α_g is set as 10% and corresponding volume fraction of water α_l equals to 90%.

VALIDATION AND VERIFICATION

Numerical model is validated in single-phase incoming water flow condition. Numerical results about lift and drag coefficients are compared with experimental (Ladson, 1988) and other numerical results (Shang and Horrillo, 2021) in literatures. Lift and drag coefficients for two-dimensional condition are shown as Eq. 14 and Eq. 15, respectively:

$$C_L = \frac{F_{lift}}{\frac{1}{2} \rho_l u_\infty^2 L} \tag{14}$$

$$C_D = \frac{F_{drag}}{\frac{1}{2} \rho_l u_\infty^2 L} \tag{15}$$

where F_{lift} and F_{drag} are lift and drag forces of the hydrofoil.

Table.2 Comparison of C_L and C_D between different methods.

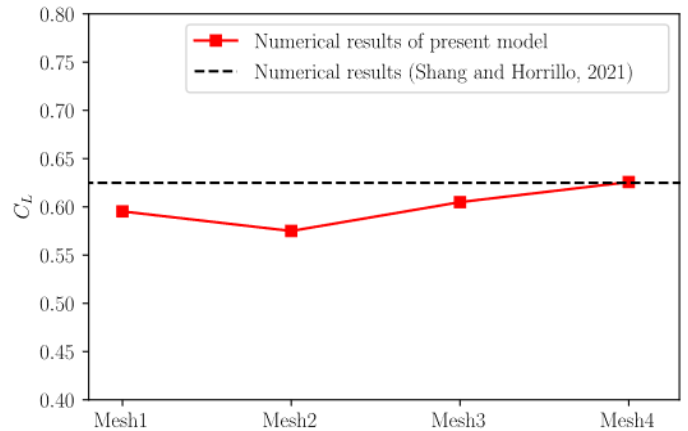
Results	C_L	C_D
Numerical results of present model	0.6049	0.0129
Numerical results (Shang and Horrillo, 2021)	0.6249	0.0130
Experimental results (Ladson, 1988)	0.6084	0.0134
Error between numerical results of present model and numerical results (Shang and Horrillo, 2021)	3.20%	0.77%
Error between numerical results of present model and experimental results (Shang and Horrillo, 2021)	0.58%	3.44%

Lift and drag coefficients calculated by present model and other

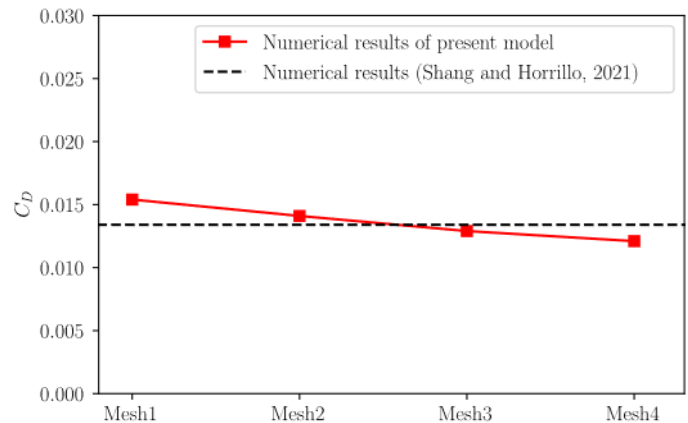
methods are summarized as Table.2. Errors between different methods are also calculated and all of errors are less than 4%. As a result, based on the comparison above, one can see that numerical results established in this paper agree well with experimental results and numerical results, which validates the numerical model.

Table.3 Mesh numbers and corresponding lift and drag coefficients.

Mesh	Total mesh number	C_L	C_D
Mesh1	27214	0.5953	0.0154
Mesh2	37 119	0.5750	0.0141
Mesh3	72 885	0.6049	0.0129
Mesh4	139 925	0.6257	0.0121



(a) Lift coefficient of different mesh sizes.



(b) Drag coefficient of different mesh sizes.

Fig.3 Mesh convergence test

Mesh convergence test is conducted to verify the convergence and robustness of this model. Proper number of the mesh is confirmed by the mesh convergence test. Four different mesh sizes are generated by changing mesh basic size and corresponding mesh number are 27214, 37 119, 72 885, and 139 925. Lift and drag coefficients for different mesh sizes are shown as Table.3 and Fig.3. One can also see the model

converges with meshes and Mesh3 is selected in this paper considering its accuracy and calculation cost.

RESULTS AND DISCUSSIONS

Comparison of Flow Fields

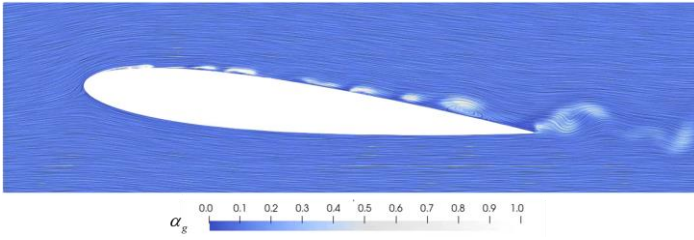
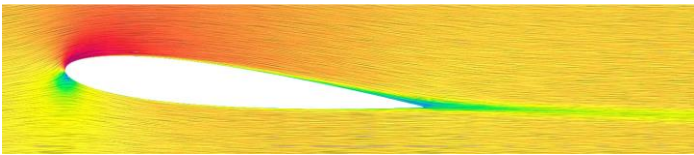
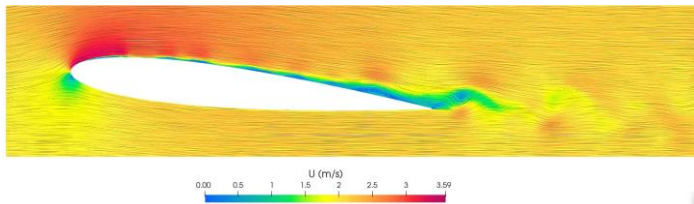


Fig.4 Instantaneous air volume fraction distribution and LIC streamline distribution near the hydrofoil at $t=7s$ for water-air-bubble mixed flow condition.

Fig.4 shows the instantaneous volume fraction distribution at $t=7s$ near the hydrofoil for water-air-bubble mixed flow condition. Instantaneous line integral convolution (LIC) is adopted to visualize the streamline and vortex distributions. The suction surface of the hydrofoil has higher air volume fraction compared to the pressure surface. The distribution of air volume fraction at the suction surface is discontinuous. One can see that vortices are generated and propagated along with higher air volume fraction. The existence of water-air-bubble flow induces the emergence of vortices.



(a) Single-phase incoming water flow condition

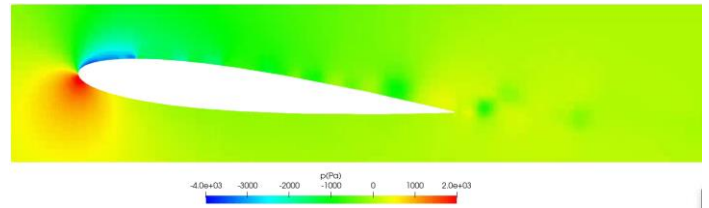


(b) Water-air-bubble mixed flow condition ($\alpha_g = 10\%$).

Fig.5 Comparison of Instantaneous LIC streamline distribution and velocity field at $t=7s$.



(a) Single-phase incoming water flow condition



(b) Water-air-bubble mixed flow condition ($\alpha_g = 10\%$).

Fig.6 Instantaneous dynamic pressure contours near the hydrofoil at $t=7s$.

Fig.5 and Fig.6 show the comparison of instantaneous velocity field and dynamic pressure contours at $t=7s$. Comparison with single-phase incoming water flow, the velocity field and dynamic pressure field show more obvious fluctuation and instability for water-air-bubble mixed incoming flow condition. More complex vortices are generated and stronger pressure fluctuation is induced due to the existence of water-air-bubble mixed flow.

Comparison of Drag and Lift Coefficients

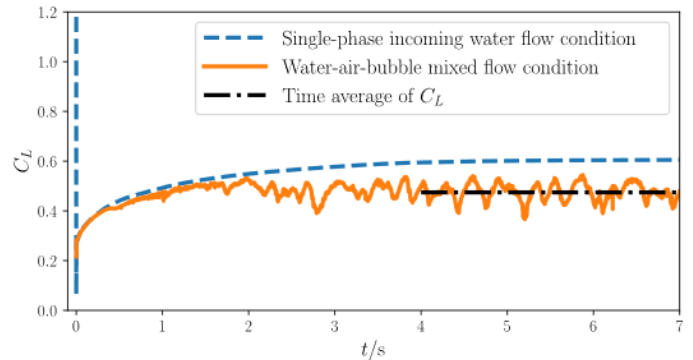


Fig.7 Comparison of time history of lift coefficient C_L .

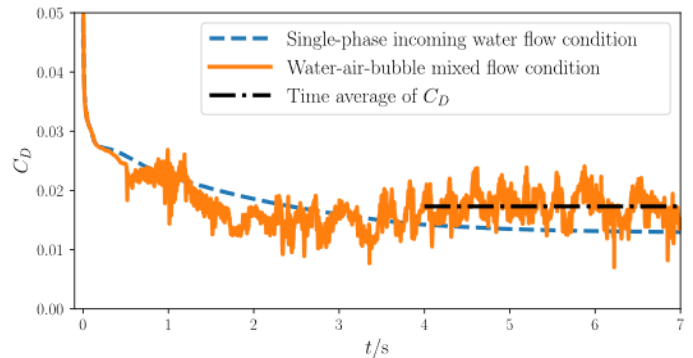


Fig.8 Comparison of time history of drag coefficient C_D .

Fig.7 and Fig.8 show the time history of lift and drag coefficient at the single-phase incoming water flow condition and water-air-bubble mixed flow condition. One can see that the time history of lift and drag coefficients show stronger oscillation at water-air-bubble mixed flow condition, which reveals stronger pressure fluctuation in Fig.6. We calculated the time average of lift and drag coefficients at the relatively stable stage, from 4s to 7s, and summarized the results as shown in Table.4. One can see that the lift coefficient decreases while the drag coefficient increases due to the water-air-bubble mixed flow.

Table.4 Comparison of lift and drag coefficients

Flow condition	C_L	C_D
Single-phase incoming water flow condition	0.6049	0.0129
Water-air-bubble mixed flow condition	0.4744	0.0173

CONCLUSIONS

In this paper, the influence of uniformly mixed water-air-bubble incoming flow on hydrodynamic performance of a two-dimensional NACA0012 hydrofoil profile is studied. TFM is adopted to solve the mixed water-air-bubble multiphase flow field around the hydrofoil. Validation about lift and drag coefficients is conducted and compared with previous experimental and numerical results for single-phase incoming water flow condition, with great agreement achieved. Mesh convergence test is conducted and further verified the convergence and robustness of this model. The effect on the flow field and lift and drag coefficients due to the mixed water-air-bubble multiphase flow is discussed. Main conclusions are summarized as follows:

- The water-air-bubble incoming flow further induced the emergence of vortices. Vortices are generated and propagated along with higher air volume fraction.
- More obvious and stronger fluctuation and instability is found for the velocity field and dynamic pressure field due to the water-air-bubble mixed incoming flow.
- The time history of lift and drag coefficients show stronger oscillation at water-air-bubble mixed incoming flow condition. The lift coefficient decreases while the drag coefficient increases due to the water-air-bubble mixed flow at the present computational conditions.

In the future, different computational conditions with different air volume fraction are calculated and analyzed to further study the effect on the hydrodynamic performance of the hydrofoil in water-air-bubble mixed flow. Population balance model is also adopted to study the coalescence and break-up process of bubbles.

ACKNOWLEDGEMENTS

This work was supported by the National Natural Science Foundation of China (52131102), and the National Key Research and Development Program of China (2019YFB1704200), to which the authors are most grateful.

REFERENCES

- Carrica, P.M., Wilson, R.V., and Stern, F. (2007). "An Unsteady Single-Phase Level Set Method for Viscous Free Surface Flows." *Int. J. Numer. Meth. Fluids*, 53, 229–256.
- Hirt, C.W., and Nichols, B.D. (1981). "Volume of Fluid (VOF) Method for the Dynamics of Free Boundaries." *Journal of computational physics*, 39, 201–225.
- Ladson, C.L. (1988). "Effects of Independent Variation of Mach and Reynolds Numbers on the Low-Speed Aerodynamic Characteristics of the NACA 0012 Airfoil Section". National Aeronautics and Space Administration, Scientific and Technical Information Division: Hampton, USA, 4074.

- Li, J., Martin, J.E., and Carrica, P.M. (2019). "Large-Scale Simulation of Ship Bubbly Wake During a Maneuver in Stratified Flow." *Ocean Engineering*, 173, 643–658.
- Ma, J., Chahine, G.L., and Hsiao, C.-T. (2015). "Spherical Bubble Dynamics in a Bubbly Medium Using an Euler–Lagrange Model." *Chemical Engineering Science* 128, 64–81.
- Ma, J., Oberai, A.A., Hyman, M.C., Drew, D.A., and Lahey, R.T. (2011). "Two-Fluid Modeling of Bubbly Flows Around Surface Ships Using a Phenomenological Subgrid Air Entrainment Model." *Computers & Fluids*, 52, 50–57.
- Mühlbauer, A., Hlawitschka, M.W., and Bart, H.-J. (2019). "Models for the Numerical Simulation of Bubble Columns: A Review." *Chem. Ing. Tech.* 91, 1747–1765.
- Schiller L., and Naumann A. (1935). "A Drag Coefficient Correlation." *Zeitschrift des Vereins Deutscher Ingenieure*, 77, 318–320.
- Shang, Y., and Horrillo, J.J., 2021. "Numerical Simulation and Hydrodynamic Performance Predicting of 2 Two-Dimensional Hydrofoils in Tandem Configuration." *Journal of Marine Science and Engineering*, 9, 462.
- Simcik, M., Ruzicka, M.C., and Drahoš, J. (2008). "Computing the Added Mass of Dispersed Particles." *Chemical Engineering Science*, 63, 4580–4595.
- Wardle, K.E., and Weller, H.G. (2013). "Hybrid Multiphase CFD Solver for Coupled Dispersed/Segregated Flows in Liquid-Liquid Extraction." *International Journal of Chemical Engineering*, 2013, 1–13.
- Zhang, D., Deen, N.G., and Kuipers, J.A.M. (2006). "Numerical Simulation of the Dynamic Flow Behavior in a Bubble Column: A Study of Closures for Turbulence and Interface Forces." *Chemical Engineering Science*, 61, 7593–7608.
- Zhang, X., Wang, J., and Wan, D. (2020). "An Improved Multi-Scale Two Phase Method for Bubbly Flows." *International Journal of Multiphase Flow*, 133, 103460.